

Characterization Alloys of the Sn-Zn System Produced by Melt Spinning

Luis Gustavo Cordioli Russi^a, Luciola Lucena de Sousa^a, Alfeu Saraiva Ramos^a,

Piter Gargarella^b, Neide Aparecida Mariano^{a*}

^aUniversidade Federal de Alfenas (UNIFAL), Rodovia José Aurélio Vilela, Poços de Caldas, MG, Brasil

^bUniversidade Federal de São Carlos, Rodovia Washington Luís, São Carlos, SP, Brasil

Received: February 18, 2019; Revised: December 31, 2019; Accepted: January 29, 2020

The objective of this work was the conformation of ribbons from Sn₃Zn alloy and Sn pure, using the melt-spinning fast cooling technique, in order to investigate the applicability as biomaterial. The ribbons were coated with 1% poly-caprolactone (PCL) and subsequent incorporation of silver nanoparticles (NPAg). In the uncoated ribbon was observing a surface roughness due of agglomerate caused by rapid solidification. In the ribbon coated with PCL and NPAg incorporation, it was observed that these compounds adhered to the ribbon. X-ray diffraction analysis showed no ribbons amorphization. The analysis by differential scanning calorimetry, indicated that the Sn₃Zn ribbon had a lower melting temperature (198.1°C) than the Sn ribbon (228.7°C). The microhardness of Sn₃Zn ribbon was 13.38 HV and Sn ribbon was 11.00 HV, both for the face without contact with the cooling wheel. In the bioactivity assays, performed in simulated body fluid medium, all samples showed apatites formation after four weeks of testing.

Keywords: melt-spinning, biomaterials, Sn-Zn alloy.

1. Introduction

Metallic meshes have been used in the reconstruction of deformations and trauma, as in oral and maxillo-facial reconstruction, for the repairing of fractures of the orbital blow-out fractures, where a collapse of the orbital floor or facial medial orbital wall occurs. For the development of this type of mesh, the material used should have the properties required to the carrying out of the function, such as mechanical resistance, malleability, toughness, resistance to corrosion and biocompatibility. Among the materials used, titanium meshes, which exhibits good osseointegration and excellent biointegration, stands out. On the other hand, the titanium meshes can lead to patient injury in the case that the patient suffers new incidents in the implanted region, possibly compromising the ocular motor capabilities due to the physical characteristics of the metal¹⁻⁴.

Polymeric materials such as polymethyl methacrylate (PMMA) and ceramic materials such as hydroxyapatites and calcium phosphate cements are also used for cranio-facial reconstruction. Hydroxyapatite (HA), in particular, as a mineral naturally present in bones, suffers minimal rejection by patients, while its osseointegration is satisfactory, being used in the guided regeneration of bone tissue and oral and maxilla-facial reconstruction and repair⁵.

For this type of use, biocompatibility and biofunctionality are required of the materials, which aim to stimulate osseointegration. The meshes of titanium and its alloys, especially Ti-6Al-4V, in addition to having these characteristics, due to its varied sizes and shapes and with thickness from

0.15 to 2mm, are classified as alloplastic, providing the conditions for making adjustments and adaptations in the mesh, to the implanted area, during the surgical intervention. This contributes to shorter surgery times and lower morbidity of the grafted area⁵⁻⁷.

There are studies which report the use of tin and Sn-Zn alloys for the composition of alloys used as biomaterials due to good resistance to corrosion, as presented by Wu et al (2005), where Sn is used in the composition of the alloy (Ti₆₀Zn₁₀Ta₁₅Si₁₅)_{100-x}Sn_x (x=0,4,8,12 at.%) for biomaterial, processed by the melt spinning method, and they observed that the increase in the concentration of Sn fostered improvement in the resistance to corrosion in a phosphate buffer solution (PBS) medium⁸.

In addition, according to Wang et al. (2013), the addition of Sn in the TiNi₃₅Si₁₅Hydroxyapatite alloy shows there was a greater growth in MC-3T3 osteoblast cells, demonstrating that the viability of cell cultivation is 0.4 times greater than in the commercially pure titanium (Tic.p.)⁹.

The use of Sn for coatings, due to the conditions of resistance to corrosion, allied with studies that prove its low toxicity, along with Zn, for its antimicrobial qualities, makes the use of its alloys as biomaterials promising^{8,9}.

The rapid solidification process by the melt spinning technique can be used to obtain amorphous metallic ribbons or ribbons with crystalline structures. It was also observed that rapid solidification improves wetting and resistance to corrosion^{10,11}.

Studies are being undertaken to improve the integration of the Sn-Zn alloys with the biological system through coating

*e-mail: neideaparecidamariano@gmail.com

techniques. Poly-caprolactone (PCL), an aliphatic polyester, is a synthetic polymer extensively used as biomaterial due to its biocompatibility, bioabsorption, low molecular weight/density and low cost^{12,13}.

Silver nanoparticles (NPAg), is inert material, used as an additive in cosmetics and medicines because of its biocidal, fungicide and germicide properties¹⁴. Incorporation of NPAg in a PCL matrix for further coating of ribbons Sn-Zn surface would be a great alternative to increase the compatibility/adhesion of PCL/ Sn-Zn.

Therefore, the aim of this work is to study the Sn-Zn alloys by melt-spinning process and the effects PCL incorporated with NPAg coatings on the ability to apatites formation on the ribbons surface, for potential application as components in maxillo-facial reconstruction. Structural, morphological and chemical characterizations of the coated of the ribbons were performed by X-ray diffraction (XRD), scanning electron microscopy (SEM), energy dispersive spectrometer (EDS) and diffuse reflectance Fourier- Transform infrared Spectroscopy (FTIR).

2. Materials and Methods

The materials used were: Sn with a degree of purity of 99.9%, produced in powder form by JBQuímica, Zn with a P.A. purity, produced by Synth, in powder form, both with an approximate grain size of 300 mesh. Poly-caprolactone (Mn 70000-90000, density 1.145 g/mL at 25°C) was purchased from Sigma- Aldrich (USA). NPAg was synthesized from a solution of 1% acetic acid, chitosan, and AgNO₃ 1.6x10⁻² M solution.

From the elements Sn and Zn the alloy was initially produced by a process of fusion in an electro-voltaic arc furnace, with a vacuum chamber, using a tungsten electrode and a water cooled copper crucible, in an inert atmosphere (argon).

The compositions of the ribbons produced were: pure Sn and Sn₃Zn (%w). The Sn₃Zn alloy was employed due to its fusion temperature being close to that of the eutectic point¹⁵ and for having a low Zn content (which exhibits anti-microbiological qualities). And, as the matrix metal of the alloy is tin, the pure Sn ribbon was used as object of comparison of the properties affected with the addition of Zn.

After the fusion, the alloy was formed into ribbons with thicknesses of around 40 µm, in the melt spinning, in a vacuum chamber, using a quartz crucible and argon atmosphere. The ribbon was cast on a copper wheel with a 200mm diameter, at a speed of 40 m/s and distance of 4mm between the crucible and the wheel. The metal load used was approximately 2g per start.

The ribbons produced were coated by PCL and PCL incorporated with NPAg. The polymeric solution was prepared by dissolving PCL in chloroform in the ratio 1:100 (w/v). The ribbons were then immersed in the solution for

03 seconds. After removal, the ribbons were dried at room temperature in a desiccator for 48 hours in order to obtain ribbon+PCL samples. The incorporation of NPAg over the surface of the ribbons with PCL covering were carried out by immersion in a solution of NPAg. After removal, the ribbons were dried at room temperature in a desiccator for 48 hours in order to obtain ribbon+PCL+NPAg samples.

The thermal analysis was performed using differential scanning calorimetry (DSC). The dynamic measurements involved two consecutive cycles at the same selected ramp rates. First, the furnace was linearly heated temperature to 300°C at heating rates of 10°C/min, using argon as carrier gas. Then, the solidification scans from 300°C at the same cooling ramps were performed.

The microstructural characterization was undertaken by scanning electron microscopy (SEM), attached to the energy dispersive spectrometer (EDS). X-ray diffraction (XRD) analyses were performed with Cu K α radiation, in a range of 2 θ from 10° to 90°, with a step of 0.02° for 2 s/step. Infrared spectroscopy analysis (FTIR) was performed using an attenuated total reflection (ATR) accessory, ribbons+PCL and ribbons+PCL+ NPAg were analyzed from 500 to 4000cm⁻¹ in order to identify the characteristic functional groups present in each sample.

The bioactivity assay was performed according to norm ISO 23317:2012¹⁶, for the ribbons covered (PCL and PCL+ NPAg) and for the ribbons without coating, with further FTIR analysis.

3. Results and Discussions

3.1 Scanning electron microscopy

Figure 1 presents the superficial characteristics of the ribbons, through scanning electron microscopy, as well as the analysis of the energy-dispersive spectroscopy for the points cited. Figure 1a refers to the superficial morphology of face of the Sn-ribbon that was in contact with the metallic wheel in cooling. It is possible to observe the deformations of the wheel-metal interface inherent to the processing melt spinning. Figure 1b presents the morphology of the face that was not in contact with the metallic wheel in cooling, and defined grains are observed.

Figures 1c and 1d are for the Sn₃Zn-Ribbon and one can observe both the face in contact with as well as that not in contact with the cooling wheel, respectively, there being a development of a matrix and agglomerates on the face that was cooled without contact with the cooling wheel. In Figure 1d, it was proved through EDS analysis that in point A (matrix region) as well as in point B (agglomerated region), the concentrations of the constituting elements stayed similar, suggesting that the compositions of these did not vary.

According to what was observed through the micrographs, the face that was not in contact with the cooling wheel was

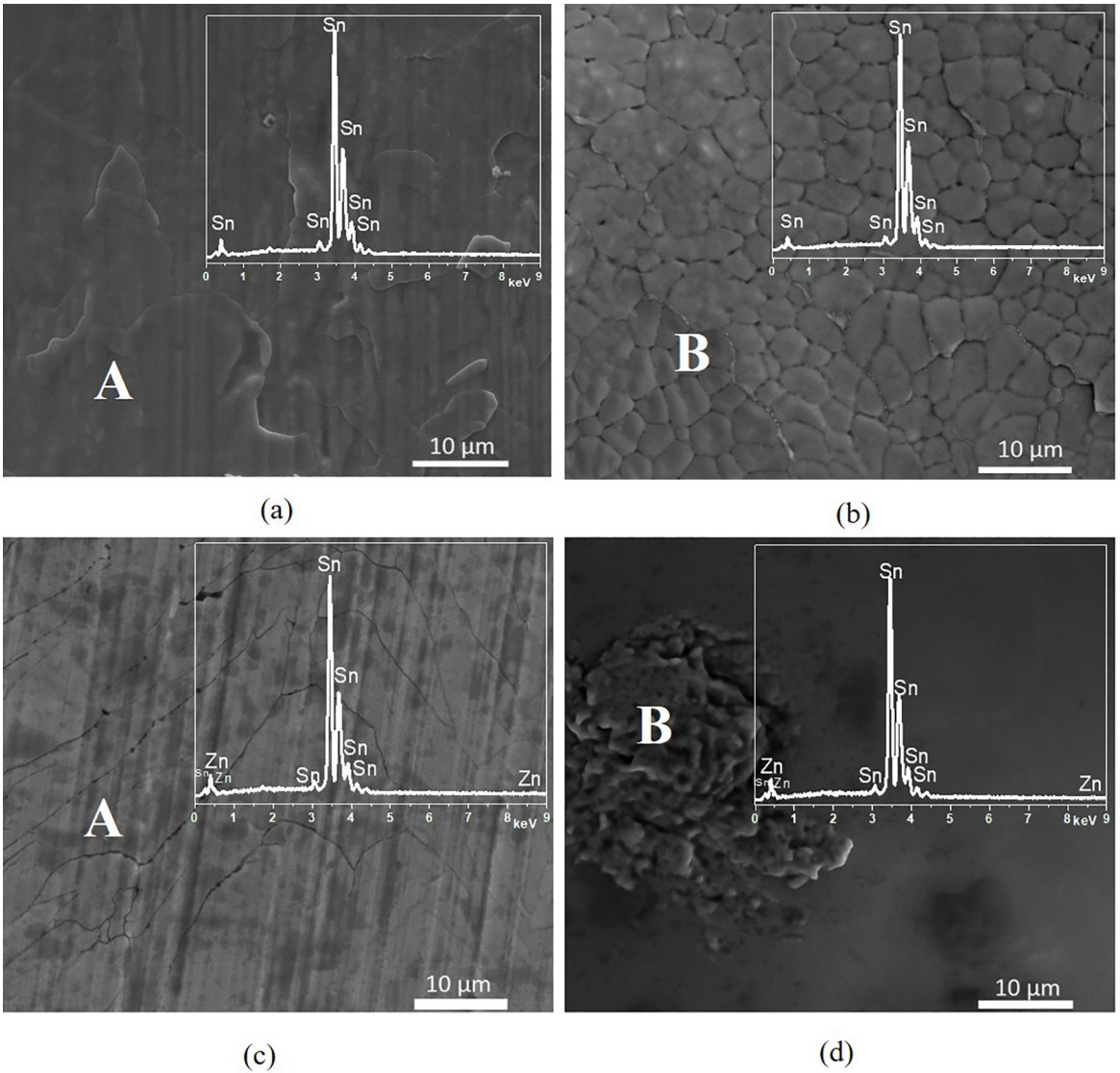


Figure 1. Micrographs obtained by Scanning Electron Microscopy and EDS spectra obtained at the points A and B: (a) Surface of Sn-ribbon, face of contact with the metal wheel on cooling; (b) Surface of Sn-ribbon, face without contact with the metal wheel on cooling; (c) Surface of Sn₃Zn-ribbon, face of contact with the metal wheel on cooling; (d) Surface of Sn₃Zn-ribbon, face without contact with the metal wheel on cooling.

adopted for the experiments due to its greater roughness, which would increase the adhesion of the coating on the metallic substrate.

According to Table 1, one can observe that the concentrations obtained by EDS were similar to those initially calculated for the composition of the ribbons.

The morphology of PCL crystals was evaluated by SEM. SEM micrographs of PCL¹⁷ and PCL+NPAg films are shown in Figures 2a and 2b, respectively. Spherulites can be observed in Figure 2a. On the other hand a smaller PCL spherulites and agglomerated de NPAg were found in PCL+NPAg film micrograph (Figure 2b).

The nucleating effect of NPAg on PCL crystallization can be confirmed by the increase of crystals amount and the reduction on the spherulites diameter. Similar EDS spectra

Table 1. Microanalysis of Sn and Sn₃Zn- ribbons obtained by EDS.

Element (%weight)	Ribbon/Alloy	
Pont A	Sn	Sn ₃ Zn
Sn	100	97.24
Zn	-	2.76
Total	100	100
Pont B		
Sn	100	97.25
Zn	-	2.75
Total	100	100

was found for PCL and PCL+NPAg films, identifying the main chemical elements found in PCL (carbon and oxygen).

The EDS spectra of Sn+PCL ribbon and Sn₃Zn+PCL ribbon (Figures 2c and 2d) indicate the presence of C and O species in both ribbons, as characteristics elements of PCL. The darkest background region observed in Figures 2c and 2d corresponds to the Sn matrix.

The EDS spectra of the Sn+PCL+NPAg ribbon and Sn₃Zn+PCL+NPAg ribbon (Figures 2d and 2e) indicate the presence of C and O elements in both ribbons, as distinctive elements of PCL, and the presence of the element Ag in both ribbons, in addition to the metallic element Sn, component of the matrix. Through the micrographs it is possible to observe the nano dimensions of the silver particles incorporated over the substrates. In both micrographs, PCL is uniformly coating all the extension of the ribbons.

3.2 X-ray diffraction

The X-ray diffractions results, obtained for the Sn and Sn₃Zn ribbons, are presented in Figure 3. The presence of alloy precursors (Sn and Zn) was observed. Amorphization of the ribbons did not occur, nor did the formation of intermetallic compounds occur, results also observed by EL-ASRAM (2006), after the formation by melt spinning¹⁸. There was no significant variation between the faces of the ribbon (the one in contact with the cooling metal wheel and the one not in contact with the wheel).

3.3 Thermal analysis

Figure 4 presents the analyses of heating by differential scanning calorimetry (DSC) for the ribbons obtained by melt spinning. The temperature at which the fusion process begins was determined by the solid state temperature (T_s), which corresponds to the initial inflection point of the endothermic peak on the DSC curve. The liquid state temperature (T_L) refers to the endothermic peak, which corresponds to the conclusion of the fusion process. The interval between these temperatures is the fusion range and determines the difference in temperature between the start of the fusion and the conclusion of the formation of liquid¹⁹.

The values of the solid state temperatures (T_s) for the Sn-ribbon and Sn₃Zn-ribbon were, respectively, 228.7 and 198.1°C, indicating the moment in which the fusion of the materials occurs. According to the DSC analysis, the liquid state temperatures (T_L) were 237.9 and 227.9°C respectively, proving that the addition of zinc to this alloy reduced the fusion temperature of the material.

3.4 Microhardness

The microhardness (HV) measures, presented in Table 2, were carried out with a 0.25 N load, and with application time of 15 seconds. The mean value refers to five measures. The microhardness measures were undertaken for both faces of the ribbon and there was not a significant variation of the values obtained. Hampshire (1990) reported that the

microhardness value of the as-cast Sn was 9.2 HV, while the values obtained for the Sn-ribbon were higher²⁰.

These results suggest that the rapid cooling interfered in the structural arrangement of the material. It was also observed that the addition of Zn fostered an increase in the microhardness values, as observed by Das et al. (2009) which obtained microhardness value of 16.8 HV for the as-cast eutectic alloy Sn₉Zn²¹. For applications as in metallic meshes used in facial grafts and as a guide for bone regeneration, there is no requirement of support for high mechanical loads. In this manner, the increase in the ribbon microhardness becomes a secondary issue.

3.5 Bioactivity

Bioactivity is a biomaterial's ability to interact with the biological medium through the formation of a thin layer of apatite (concentrations of calcium and phosphorus), that interact through chemical bonds with bone tissue and implanted material, promoting osseointegration and reducing rejection of the implanted material. Apatites, in general, have variations in their chemical formulation, which can be identified through the atomic ratio Ca/P, for the most frequent types.

Hydroxyapatite (HA), $\text{Ca}_{10}(\text{PO}_4)_6(\text{OH})_2$ is one of the apatites formed and represents around 30-70% of the composition of the bone. It is the most stable and least soluble mineral among the apatites. The Ca/P atomic ratio is approximately 1.67. HA possesses biocompatibility and bioactivity properties, favorable for bone growth in implanted locations, that is, it is osteoconductive²²⁻²⁴.

The bioactivity trial describes the capacity for apatite formation over the surface of metallic implants, in SBF solution, for a period of four weeks¹⁶. The analyses were done through SEM for the first and fourth weeks of trials. FTIR for the four weeks and for the sample that did not undergo trial. In this manner, it is possible to assess the evolution in the formation of apatites over the surface of the metallic substrate.

Figure 5 presents SEM of the surface of the Sn-Ribbon, Sn+PCL-Ribbon and Sn+PCL+NPAg-Ribbon during the first and fourth weeks of the bioactivity trials, as well as the semi quantitative analysis by EDS for points A identified in the images.

In Figure 5a, the first week of essay, there was no apatite formation activity on the surface of the Sn-Ribbon and, despite the presence of calcium (Ca) and oxygen (O), there are no peaks relating to phosphorus (P), suggesting that the analyzed region exhibited a low rate of homogeneity of the element^{16,25}. Figure 5b demonstrates the formation of more uniform apatite structures on the surface of the ribbon, with the presence of distributed apatite mineralization nodule, in predominantly globular form, with diameters around 3µm, with cracks and overlapping of layers on the surface.

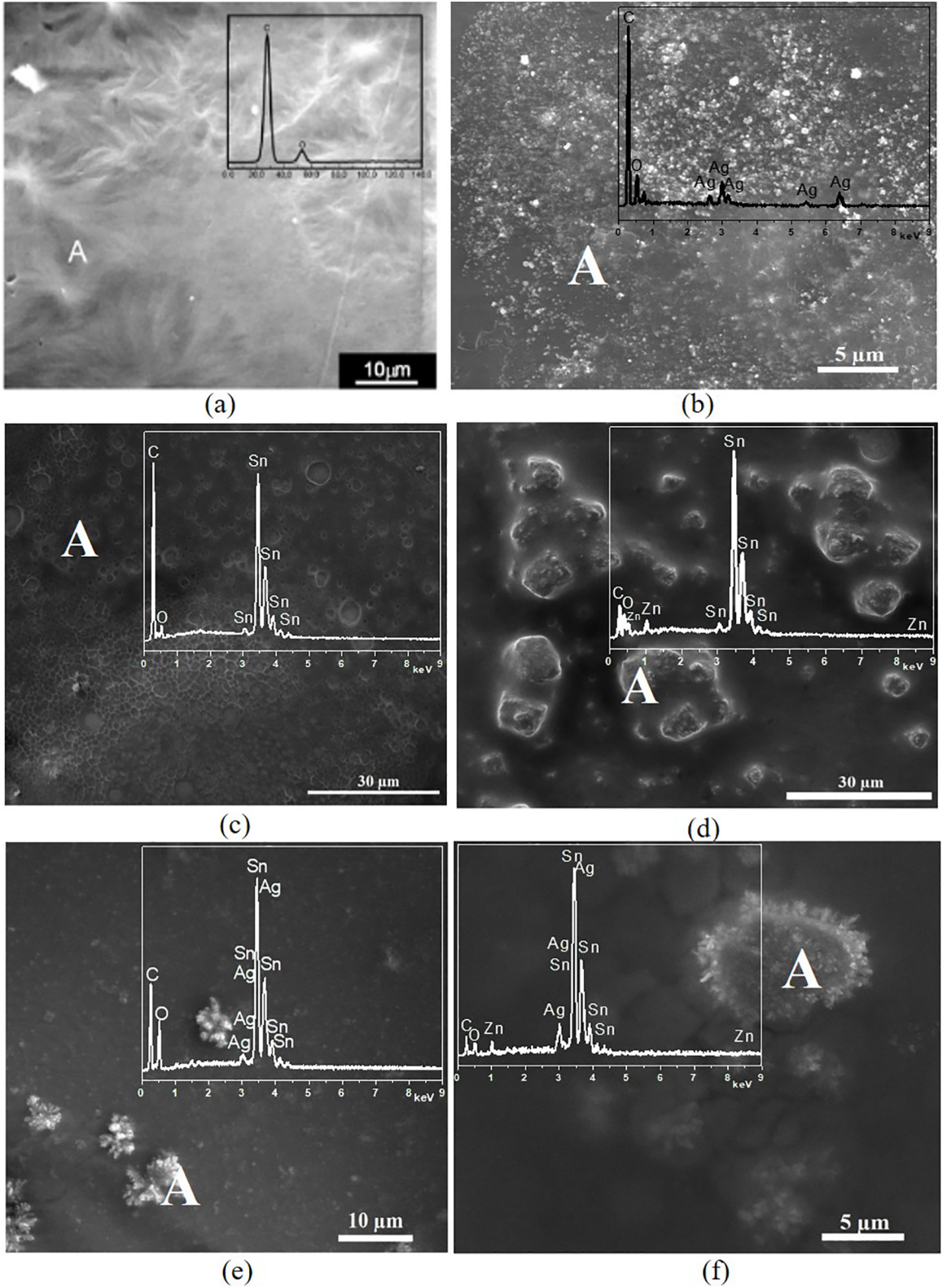


Figure 2. Micrographs obtained by Scanning Electron Microscopy and EDS spectra obtained at the point A: (a) PCL film¹⁷; (b) PCL+NPAg-ribbon; (c) Sn+PCL-ribbon; (d) Sn₃Zn+PCL-ribbon; (e) Sn+PCL+NPAg-ribbon; (f) Sn₃Zn+PCL+NPAg-ribbon.

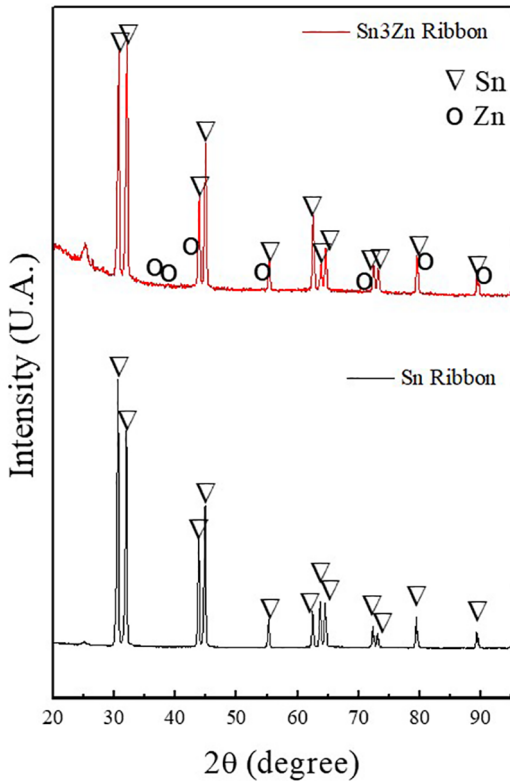


Figure 3. X-ray Diffractograms of (black) Sn ribbons and (red) Sn3Zn ribbons.

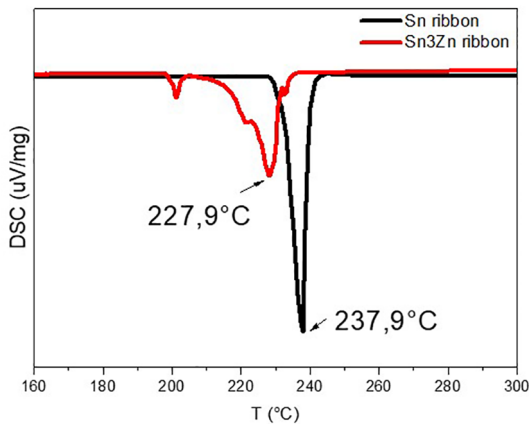


Figure 4. Differential Scanning Calorimetry curves of (black) Sn-ribbons and (red) Sn3Zn ribbons.

Table 2. Microhardness (HV) measurements of Sn and Sn3Zn- ribbons.

Ribbon/Alloy	microhardness (HV)
Sn-ribbon – Face of contact with the metal wheel on cooling	12.20±0.78
Sn-ribbon – Face without contact with the metal wheel on cooling	11.00±0.90
Sn3Zn-ribbon – Face of contact with the metal wheel on cooling	14.86±0.31
Sn3Zn-ribbon – Face without contact with the metal wheel on cooling	13.38±1.60

From the EDS analysis, carried out at point A of Figure 5b, an atomic ratio of Ca by P, with a value of 1.39 was obtained, proving that the formation of hydroxyapatite on the ribbon did not occur¹⁶. The rates of sodium (Na), magnesium (Mg) and chlorine (Cl) present in the EDS analyses stem from the SBF solution. The elements carbon (C) and oxygen (O) can be a result of contamination of the samples by organic material.

Figures 5c and 5d present the micrographs by SEM and EDS for the Sn+PCL-Ribbons, in the first and fourth weeks, respectively. The formation of the characteristic PCL film and a depositing of apatites already in the first week of trial were observed. In the analysis by EDS, the presence of peaks distinctive of phosphorus (P), Calcium (Ca) and oxygen (O) were observed. In Figure 5d corresponding to the fourth week of assay, one can observe the presence of several layers of apatite mineralization nodules, in globular form, with diameters of 3-5 μm . The atomic ratio, found in the EDS analysis, between Ca/P was 1.34, proving that the formation of hydroxyapatite did not occur¹⁶. The presence of C (carbon) and O (oxygen) elements in both EDS spectra, as elements characteristic of PCL. The presence of sodium (Na) and chlorine (Cl) stem from the SBF solution.

Figures 5e and 5f present the micrographs by SEM and EDS for the Sn+PCL+NPAg-Ribbon and the PCL film over the Sn substrate and agglomerates composed of NPAg were observed. In the analysis by EDS, the presence of Ag (silver) over the analyzed region occurred, as well as the presence of phosphorus (P), calcium (Ca) and oxygen (O) relating to the apatite formation activity, in addition to carbon (C) and oxygen (O) relating to the PCL film and the presence of sodium (Na), magnesium (Mg) and chlorine (Cl) stemming from the SBF solution. In the fourth week of the assay, presented in Figure 5f, the formation of apatite with a globular structure was observed, with, according to the concentrations obtained by EDS, a Ca/P atomic ratio of 1.44. The formation of hydroxyapatite did not occur, however.

Through the FTIR analyses, presented in Figure 6, it was possible to observe the distinctive bands of the groups relating to the apatite formation.

The FTIR spectra in Figure 6a refer to the Sn-Ribbon and show the bands located at 3643, 1480, 1400 cm^{-1} which are related, respectively, to the bands distinctive of the OH group, the type A CO_3^{2-} group and to the asymmetrical stretching of the carbon bond of the type B CO_3^{2-} group indicating, thus, the formation of apatites. The PO_4^{3-} groups are identified in the bands situated at 1150, 1020 e 590 cm^{-1} , this relating to the vibration of the asymmetrical bond of the phosphate²⁶. In the control ribbon (week 0), these bands are not evident, indicating that the formation of apatite mineralization nodules did not occur.

In Figure 6b the bands located at 3640, 1490, 1420 cm^{-1} are related, respectively, to the bands distinctive of the OH group, the type A CO_3^{2-} group and to the asymmetrical

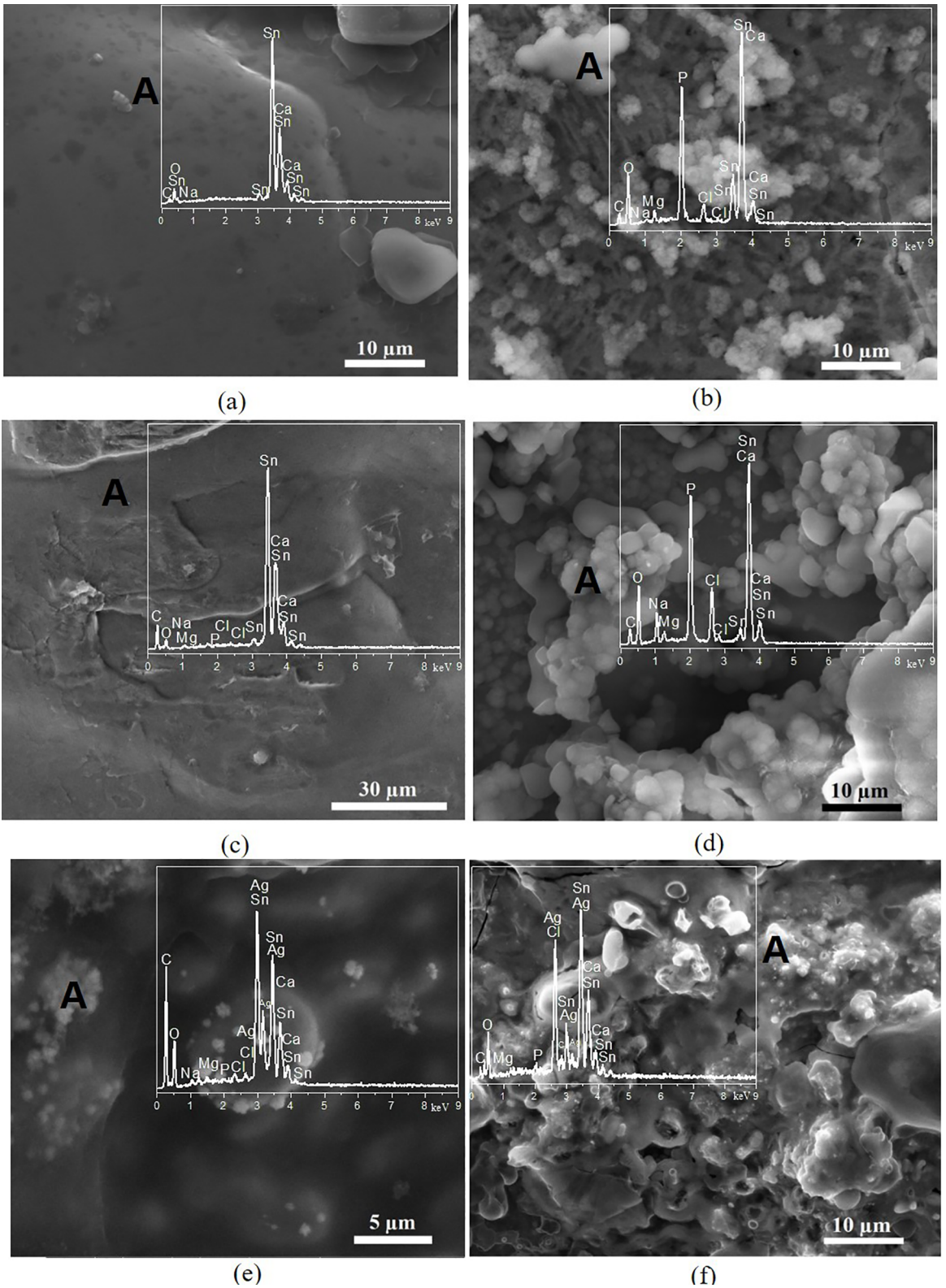


Figure 5. Micrographs obtained by SEM and EDS spectra obtained at the point A. Bioactivity assay. (a) Sn-ribbon-1st week; (b) Sn-ribbon-4th week; (c) Sn+PCL ribbon-1st week; (d) Sn+PCL ribbon-4th week; (e) Sn+PCL+NPAg-ribbon-1st week; (f) Sn+PCL+NPAg-ribbon-4th week.

stretching of the type B CO_3^{2-} group carbon bonds, indicating the formation of apatites. The PO_4^{3-} groups are identified in the bands situated²⁶ at 1140, 1020 and 565 cm^{-1} . On the reference ribbon (week 0), only the bands distinctive of the PCL film were observed. The absorption bands in the range of 2862 and 2942 cm^{-1} are due to the deformation of CH_2 of the PCL, interconnected to the inorganic network. The band at 1726 cm^{-1} is attributed to the stretching vibration of the carbonyl groups ($\text{C}=\text{O}$) present in the PCL. Among the characteristic vibrations of the PCL, the absorption bands 1233, 1107 and 1042 cm^{-1} correspond to the asymmetric COC vibration^{12,17,27}.

Through the FTIR spectrum for the Sn+PCL+NPAg Ribbon, Figure 6c, the bands located at 3610, 1500, 1412 cm^{-1} , are respectively related to the bands distinctive of the OH group, the types A and B CO_3^{2-} groups, indicating the formation of apatites. The PO_4^{3-} groups are identified in the bands situated at 1140, 1030 and 590 cm^{-1} , these bands are more pronounced in weeks one through four²⁶. In control ribbon (week 0) the bands are not evident, indicating the non-formation of mineralization nodules in this apatite situation.

On the reference ribbon (week 0), only the bands distinctive of PCL film were observed. The absorption bands in the range of 2862 and 2942 cm^{-1} are due to the deformation of CH_2 of the PCL interconnected to the inorganic network. The band at 1726 cm^{-1} is attributed to the stretching vibration of the carbonyl groups ($\text{C}=\text{O}$) present in the PCL. Among the distinctive vibrations of the PCL, the absorption bands 1233, 1107 and 1042 cm^{-1} correspond to the asymmetric COC vibration^{12,17,27}.

Figure 7 presents the SEM/EDS for the Sn3Zn-Ribbon, the Sn3Zn+PCL-Ribbon and the Sn3Zn+PCL+NPAg-Ribbon during the bioactivity assay. One can observe in Figure 7a, first week, the presence of apatite-forming activity, proved by the presence of phosphorus (P), calcium (Ca) and oxygen (O) in the EDS analysis. The largest apatite-forming activity is proven in Figure 7b, corresponding to the fourth week of assay, where the formation of mineralization nodules, with diameters of approximately 3 μm , is clear. However, through the EDS analysis, the atomic ratio of the elements Ca and P are different from 1.67, suggesting that there was no formation of hydroxyapatite over the analyzed region¹⁶.

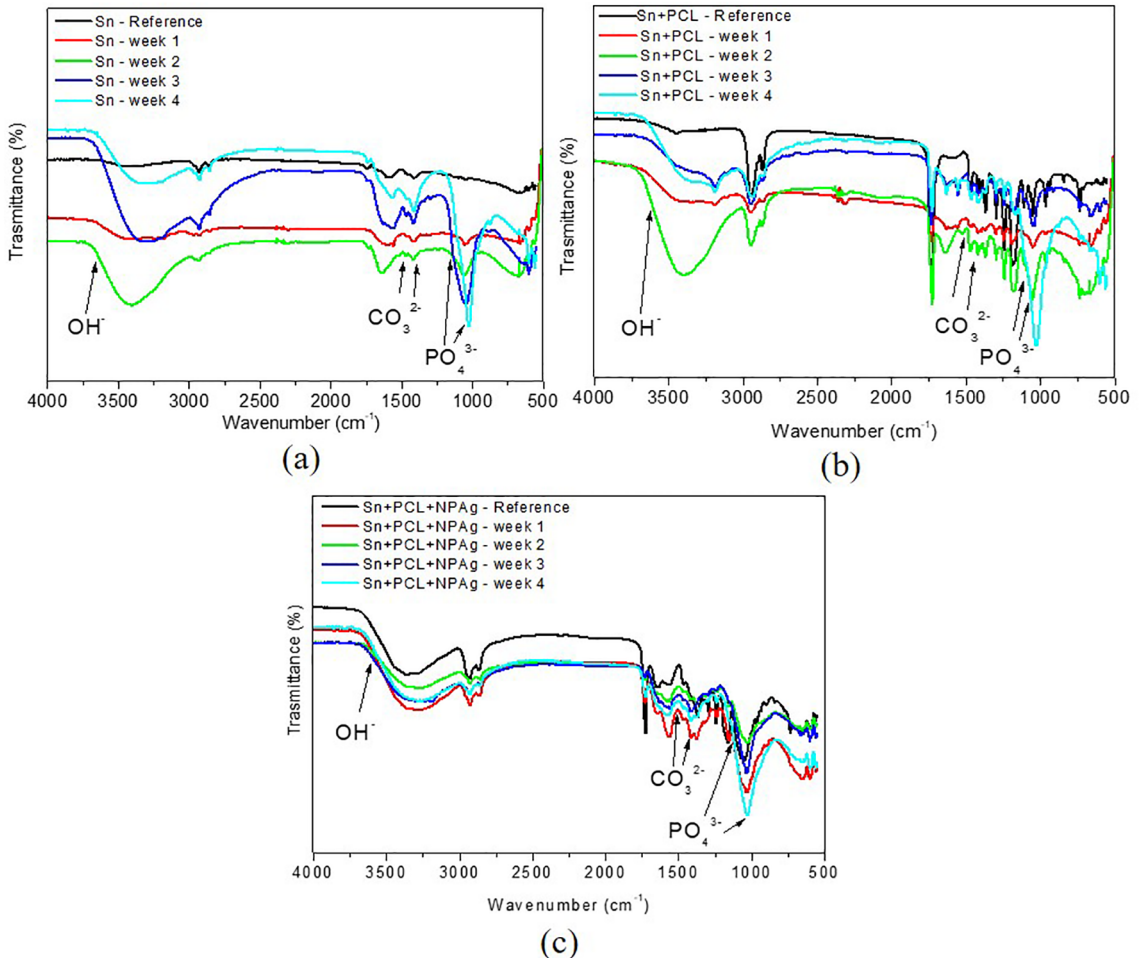


Figure 6. FTIR analysis after bioactivity assay. (a) Sn-ribbon, (b) Sn+PCL-ribbons and (c) Sn+PCL+NPAg- ribbons.

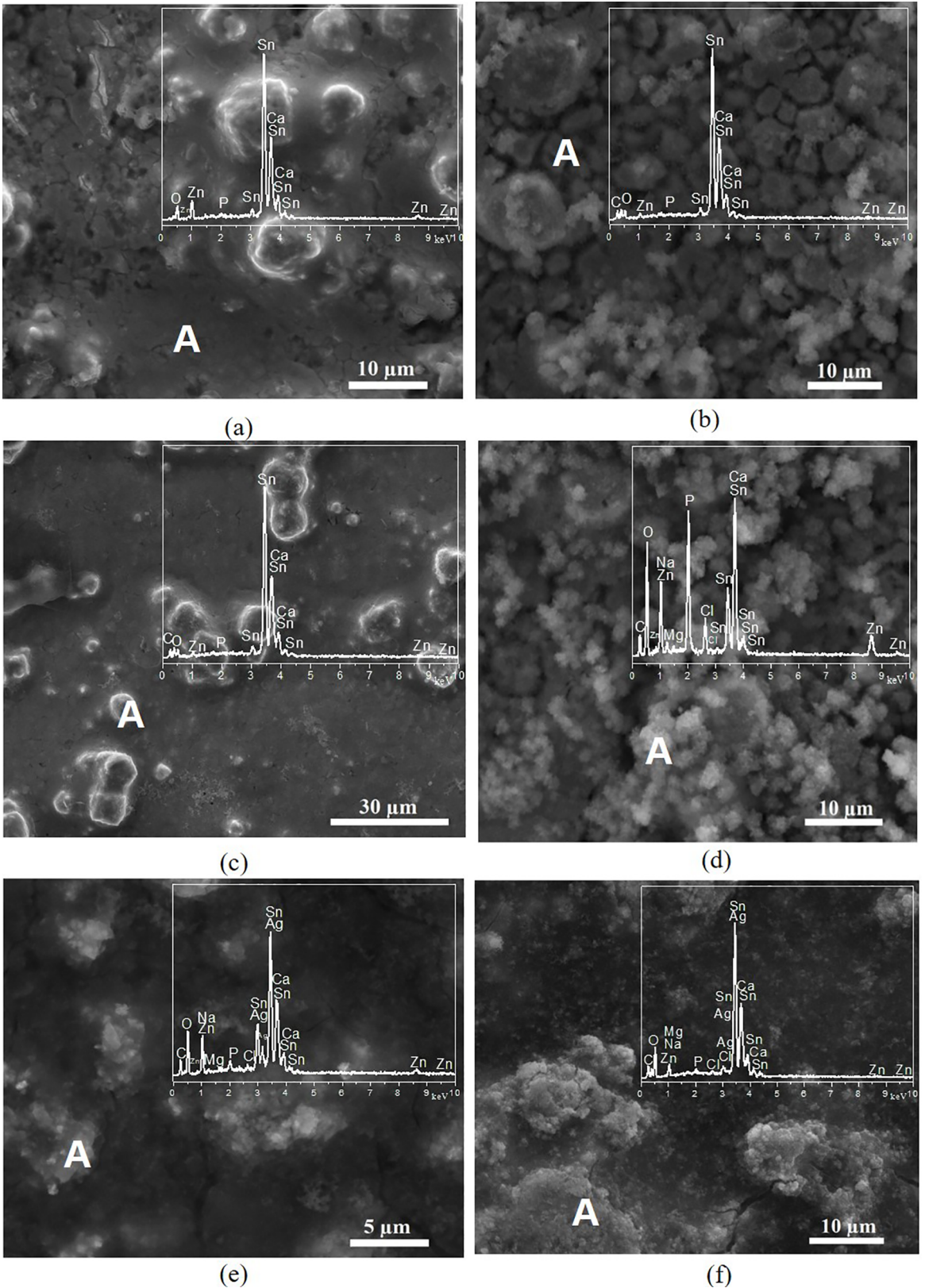


Figure 7. Micrographs obtained by SEM and EDS spectra obtained at the point A. Bioactivity assay. (a) Sn3Zn-ribbon-1st week; (b) Sn3Zn-ribbon-4th week; (c) Sn3Zn+PCL ribbon-1st week; (d) Sn3Zn+PCL ribbon-4th week; (e) Sn3Zn+PCL+NPAg-ribbon-1st week; (f) Sn3Zn+PCL+NPAg-ribbon-4th week.

Figure 7c shows the micrograph for the first assay week of the Sn3Zn+PCL-Ribbon and aspects characteristic of apatite formation were observed, due to the presence of the elements phosphorus (P), calcium (Ca) and oxygen (O) in the EDS analysis. In the fourth assay week, Figure 7d, an irregular formation of apatite mineralization nodules over the substrate occurred, in globular form, with diameter of 3 μm . The activity was proved by the EDS analysis, with peaks distinctive of the elements. The Ca/P atomic ratio was 1.25, there being no hydroxyapatite formation¹⁶. In the fourth week EDS spectrum the presence of carbon (C) and oxygen (O) due to the PCL film was also observed, as well as the presence of sodium (Na), magnesium (Mg) and chlorine (Cl) derived from the SBF solution.

The qualities present on the surface of the Sn3Zn+PCL+NPAg-Ribbon, after the first week of assay, are present in Figure 7e and the formation of structures stemming from the mineralization of apatites were observed. Due to the presence of distinctive elements such as phosphorus (P), calcium (Ca) and oxygen (O), observed in the EDS analysis. In the fourth assay week, Figure 7f, there is an intensification of the phosphorus (P) and calcium (Ca) peaks, which proves

that the activity in the fourth week is greater than that of the first week.

The Ca/P atomic ratio was 1.66, which suggests that the formation of hydroxyapatite occurred in the region analyzed by EDS¹⁶. In the EDS spectrum of the fourth week, the presence of sodium (Na), magnesium (Mg) and chlorine (Cl) stemming from the SBF solution, was observed, and carbon (C) and oxygen (O) due to the PCL film and silver (Ag) due to incorporation into the PCL film.

Through the FTIR spectra for the Sn3Zn-Ribbon, Figure 8a, the bands located at 3620, 1490, 1407 cm^{-1} , are related, respectively, to the bands distinctive of the OH group, the type A CO_3^{2-} group, and to the asymmetric stretching of the carbon bond of the type B CO_3^{2-} group, indicating, in this manner, the formation of apatites. The PO_4^{3-} groups are identified in the bands situated²⁵ at 1175, 1024 e 545 cm^{-1} . In the reference ribbon (week 0) the bands are not highlighted, indicating the non-formation of mineralization nodules in that apatite situation.

According to the infrared spectra, Figure 8b, undertaken during the bioactivity assay, one observed bands distinctive of the OH⁻ group at 3660 cm^{-1} , of the type A CO_3^{2-} group

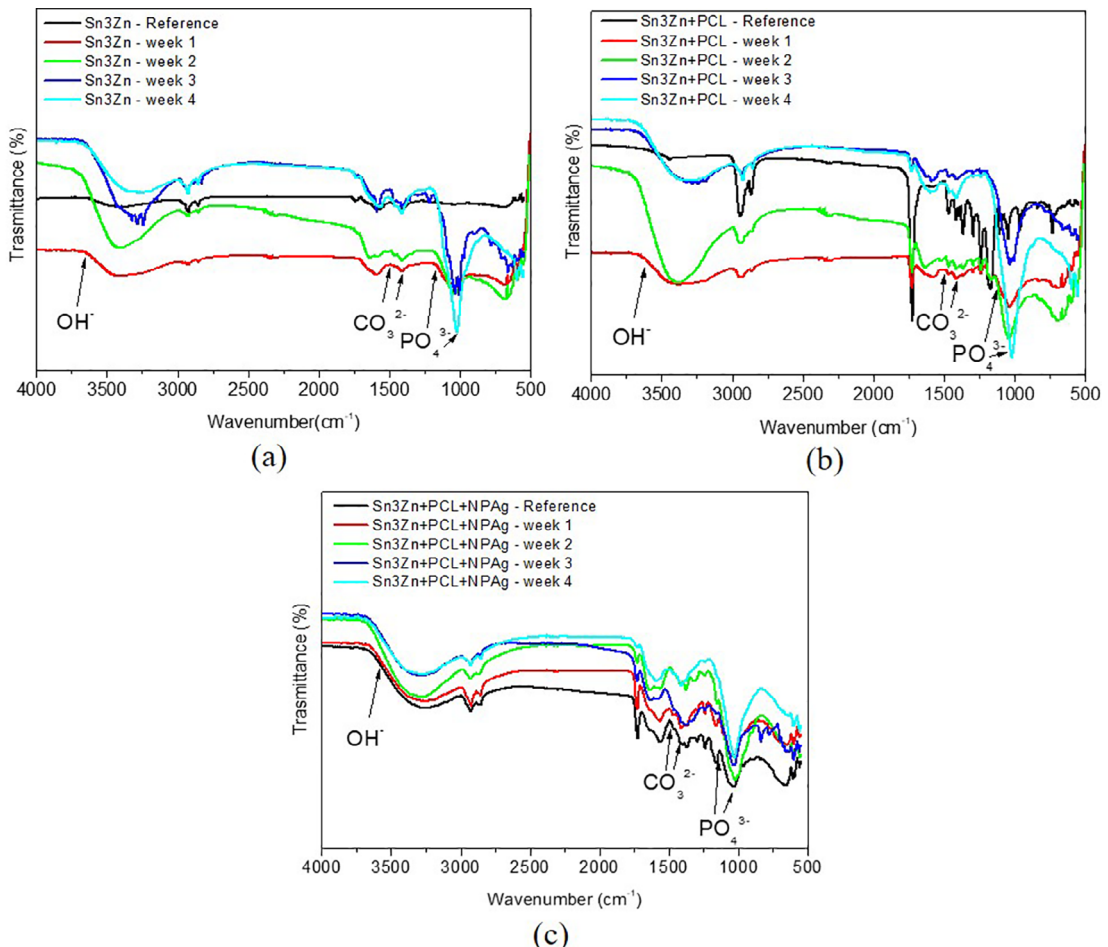


Figure 8. FTIR analysis after bioactivity assay. (a) Sn3Zn-ribbon, (b) Sn3Zn+PCL-ribbon and (c) Sn3Zn+PCL+NPAg-ribbon.

at 1478 cm^{-1} and type B at 1412 cm^{-1} , corresponding to the asymmetric stretching of the carbon bond, indicating the formation of apatites over the tested substrate. The PO_4^{3-} groups are identified in the bands located²⁵ at 1130, 1020 and 560 cm^{-1} . On the reference band (week 0), the bands observed were distinctive of the PCL film. The absorption bands in the range of 2862 and 2942 cm^{-1} are due to the deformation of CH_2 of the PCL, interconnected to the inorganic network. The band at 1726 cm^{-1} is attributed to the stretching vibration of the carbonyl groups (C=O) present in the PCL. Among the distinctive vibrations of the PCL, the absorption bands 1233, 1107 and 1042 cm^{-1} correspond to the asymmetric COC vibration^{12,17,27}.

According to the infrared spectra, Figure 8c, undertaken during the bioactivity assay, one observed bands distinctive of the OH⁻ group at 3620 cm^{-1} , of type A CO_3^{2-} group at 1480 cm^{-1} and type B at 1417 cm^{-1} , corresponding to the asymmetric stretching of the carbon bonds, indicating the formation of apatites. The PO_4^{3-} groups are identified in the bands situated²⁵ at 1150, 1022 and 583 cm^{-1} .

On the reference ribbon (week 0), the bands observed were those distinctive of the PCL film. The absorption bands in the range of 2862 and 2942 cm^{-1} are due to the deformation of CH_2 of the PCL interconnected to the inorganic network. The band at 1726 cm^{-1} is attributed to the stretching vibration of the carbonyl groups (C=O) present in the PCL. Among the characteristic vibrations of the PCL, the absorption bands 1233, 1107 and 1042 cm^{-1} correspond to the asymmetric COC vibration^{12,17,27}.

4. Conclusions

The micrographs of the ribbons demonstrated that the formation of agglomerates on the surface occurred, resulting from the high rate of solidification and nucleation, preventing the uniform dispersal of the liquid metal over the surface, observing that the refinement of the grains took place, due to the high rate of cooling. The roughness formed by the superficial agglomerates can contribute to the adhesion process of the metallic material to the bone tissue. The micrographs showed, also, that the PCL covering as well as the subsequent incorporating of the NPAg adhered to the metal substrate, which enables the incorporation of drugs in the polymeric surface, helping in the recovery of the implanted area. The differential scanning calorimetry analysis showed reduction of the temperature band of the Sn3Zn-ribbon melting, compared to the Sn-ribbon, confirming that the inclusion of Zn in the alloy contributes to the reduction in melting temperature. The microhardness assay demonstrated that, with the addition of Zn, the microhardness of the ribbon increases, ensuring the implant greater resistance to mechanical stress during use, even if this parameter is not paramount for the purpose of ribbons as metal mesh. The bioactivity assay demonstrated that there was apatite-forming activity on the surface in the

conditions studied. And the Sn3Zn+PCL+NPAg-ribbon presented a Ca/P relationship corresponding to the formation of hydroxyapatites, which contributes to better interaction in the implant-bone interface, acting more significantly in osseointegration.

5. Acknowledgements

The authors thank Brazilian research funding agencies FAPEMIG, CNPq, FINEP and CAPES for financial.

Referências

- Jegham H, Masmoundi R, Ouertani H, Blouza I, Turki S, Khattech MB. Ridge augmentation with titanium mesh: a case report. *Journal of Stomatology, Oral and Maxillofacial Surgery*. 2017;118(3):181-186.
- Her S, Kang T, Fien MJ. Titanium mesh as an alternative to a membrane for ridge augmentation. *Journal of Oral and Maxillofacial Surgery*. 2012;70(4):803-810.
- Cortez ALV, Rabelo GO, Mazzonetto R. Reconstrução de maxila atrófica utilizando osso autógeno e malha de titânio para posterior reabilitação com implantes – caso clínico. *Revista Portuguesa de Estomatologia, Medicina Dentária e Cirurgia Maxilofacial*. 2004;45(3):163-167.
- Thomas P. Clinical and diagnostic challenges of metal implant allergy using the example of orthopedic surgical implants. *Allergo Journal International*. 2014;23(6):179-185.
- Gluckman H, Du Toit J. Guided bone regeneration using a titanium membrane at implant placement: a case report and literature discussion. *International Dentistry*. 2014;4(6):20-29.
- Ortega-Lopes R, Netto HDMC, Nascimento FFAO, Klüppel LE, Stabile GAV, Mazzonetto R. Reconstrução alveolar com enxerto ósseo autógeno e malha de titânio: análise de 16 casos. *Revista Implantnews*. 2010;7(1):73-80.
- Bionnovation Implantes e Biomateriais. *Catálogo de produtos*. Bauru: Bionnovation; 2017-2019; [access in 2017 mar 03]. Available from: <http://bionnovation.com.br/catalogo.html>
- Wu XQ, Peng Q, Zhao JC, Lin JG. Effect of Sn content on the corrosion behavior of Ti-based biomedical amorphous alloys. *International Journal of Electrochemical Science*. 2015;10(3):2045-2054.
- Wang X, Chen Y, Xu L, Liu Z, Woo KD. Effects of Sn content on the microstructure, mechanical properties and biocompatibility of Ti-Nb-Sn/hydroxyapatite biocomposites synthesized by powder metallurgy. *Materials and Design*. 2013;49(1):511-519.
- Tsao LC. Effect of Sn addition on the corrosion behavior of Ti-7Cu-Sn cast alloys for biomaterial applications. *Materials Science and Engineering: C*. 2015;46(1):246-252.
- Zhang W, Li M, Chen Q, Hu W, Zhang W, Xin W. Effects of Sr and Sn on microstructure and corrosion resistance of Mg-Zr-Ca magnesium alloy for biomedical applications. *Materials and Design*. 2012;39(1):379-383.

12. Catauro M, Bollino F, Papale F. Surface modifications of titanium implants by coating with bioactive and biocompatible poly (ϵ -caprolactone)/SiO₂ hybrids synthesized via sol-gel. *Arabian Journal of Chemistry*. 2015;11(7):1126-1133.
13. Smith CM, Roy TD, Bhalkikar A, Li B, Hickman JJ, Church KH. Engineering a titanium and polycaprolactone construct for a biocompatible interface between the body and artificial limb. *Tissue Engineering Part A*. 2010;16(2):717-724.
14. Zhang XF, Liu ZG, Shen W, Gurunathan S. Silver nanoparticles: synthesis, characterization, properties, application and therapeutic approaches. *International Journal of Molecular Sciences*. 2016;17(9):1534-1568.
15. Baker H. Alloy phase diagrams. In: Okamoto H, Schlesinger ME, Mueller EM, eds. *ASM handbook: Metals handbook*. Ohio: ASM International; 1992. v. 3. p. 1442.
16. International Organization for Standardization (ISO). *ISO 23317:2012 – Implants for surgery – In vitro evaluation for apatite-forming ability of implant materials*. Geneva: ISO; 2012.
17. Ferreira CC, Ricci VP, Sousa LL, Mariano NA, Campos MGN. Improvement of titanium corrosion resistance by coating with poly-caprolactone and poly-caprolactone/titanium dioxide: potential application in heart valves. *Materials Research*. 2017;20(Suppl 1):126-33.
18. El-Ashram T. Structure and properties of rapidly solidified pure tin. *Radiation Effects and Defects in Solids*. 2006;161(3):193-197.
19. Byrne CJ, Weinstein SJ, Steen PH. Capillary stability limits for liquid metal in melt spinning. *Chemical Engineering Science*. 2006;61(24):8004-8009.
20. Hampshire WB. Tin and tin alloys, properties and selection: nonferrous alloy and special-purpose materials. In: ASM International. *Properties and selection: nonferrous alloys and special-purpose materials*. ASM Handbook. Ohio: ASM International; 1990. v. 2. p. 1589-1618.
21. Das SK, Sharif A, Chan YC, Wong NB, Yung WKC. Influence of small amount of Al and Cu on the microstructure, microhardness and tensile properties of Sn-9Zn binary eutectic solder alloy. *Journal of Alloys and Compounds*. 2009;481(1-2):167-172.
22. Nayar S, Sinha MK, Basu D, Sinha A. Synthesis and sintering of biomimetic hydroxyapatite nanoparticles for biomedical applications. *Journal of Materials Science: Materials in Medicine*. 2006;17:1063-1068.
23. Angelescu N, Ungureanu DN, Anghelina FV. Synthesis and characterization of Hydroxyapatite obtained in different experimental conditions. *The Scientific Bulletin of Valahia University – Materials and Mechanics*. 2011;6(9):15-18.
24. Kuroda K, Okido M. Hydroxyapatite coating of titanium implants using hydroprocessing and evaluation of their osteoconductivity. *Bioinorganic Chemistry and Applications*. 2012;2012:730693.
25. Abe Y, Kokubo T, Yamamuro T. Apatite coating on ceramics, metals and polymers utilizing a biological process. *Journal of Materials Science: Materials in Medicine*. 1990;1:536-540.
26. Bulina NV, Chaikina MV, Prosanov IY, Dudina DV, Solovyov LA. Fast synthesis of La-substituted apatite by the dry mechanochemical method and analysis of its structure. *Journal of Solid State Chemistry*. 2017;252(1):93-99.
27. Catauro M, Bollino F, Veronesi P, Lamanna G. Influence of PCL on mechanical properties and bioactivity of ZrO₂-based hybrid coatings synthesized by sol-gel dip coating technique. *Materials Science and Engineering: C*. 2014;39:344-351.